Symmetry-Breaking Phase Transitions, Dielectric and Magnetic properties of Pyrrolidinium-Tetrahalidocobaltates

Journal:	*Inorganic Chemistry Frontiers*
Manuscript ID	QI-RES-01-2022-000187.R1
Article Type:	Research Article
Date Submitted by the Author:	11-Mar-2022
Complete List of Authors:	Ksiądzyna, Martyna; University of Wrocław, Faculty of Chemistry Kinzhybalo, Vasyl; W. Trzebiatowski Institute of Low Temperature and Structure Research Polish Academy of Sciences in Wrocław, Bieńko, Alina; University of Wroclaw, Faculty of Chemistry Medycki, Wojciech; PAS, Institute of Molecular Physics Jakubas, Ryszard; University of Wroclaw, Faculty of Chemistry Rajnák, Cyril; University of SS Cyril and Methodius, Department of Chemistry Boca, Roman; University of SS Cyril and Methodius, Department of Chemistry Ozarowski, Andrew; Florida State University, National High Magnetic Field Laboratory Ozerov, Mykhaylo; Florida State University, National High Magnetic Field Laboratory Piecha-Bisiorek, Anna; University of Wrocław, Faculty of Chemistry

Symmetry-Breaking Phase Transitions, Dielectric and Magnetic properties of Pyrrolidinium-Tetrahalidocobaltates

Martyna Ksiądzyna(a), Vasyl Kinzhybalo(b), Alina Bieńko(a), Wojciech Medycki(c), Ryszard Jakubas(a), Cyril Rajnák(d), Roman Boča(d), Andrew Ozarowski[e], Mykhaylo Ozerov[e], Anna Piecha-Bisiorek(a)*

(a) *Faculty of Chemistry, University of Wrocław, F. Joliot-Curie 14, 50-383 Wrocław, Poland*
(b) *Institute of Low Temperature and Structure Research Polish Academy of Sciences, Okólna 2, 50-422 Wrocław, Poland*
(c) *Institute of Molecular Physics, Polish Academy of Sciences, M. Smoluchowskiego 17, 60-179 Poznań, Poland*
(d) *Department of Chemistry, Faculty of Natural Sciences, University of SS Cyril and Methodius, 91701 Trnava, Slovakia*
(e) *National High Magnetic Field Laboratory, Florida State University, 1800 East Paul Dirac Drive, Tallahassee, Florida 32310,United States*

Abstract

We report the physicochemical characteristics of novel Co-based pyrrolidinium analogs: $(C_4H_{10}N)_2CoCl_4$ (**PCC**) and $(C_4H_{10}N)_2CoBr_4$ (**PCB**). Both compounds consist of the zero-dimensional (OD) anionic network and disordered pyrolidinium cations. The structural origin of the anomalies observed in the electrical measurements, has been confirmed by DSC thermograms and X-ray analysis. The crystals under investigations undergo complex sequence of phase transitions; **PCC** at 347/353 K (phase **I** ↔ phase **II**) and 202/257 K (**II** ↔ **III**) whereas **PCB** at 380/381 K (**I** ↔ **II**) and 256/302 K (**II** ↔ **III**). Molecular motions of cations in both compounds were analysed based on the proton magnetic resonance (^{1}H NMR and M_2) measurements, while magnetic properties were investigated in DC and AC modes. The DC data shows magnetic anisotropy, which was confirmed by high-field HF EPR measurements. The AC susceptibility data of **PCC** reveal slow magnetic relaxation at the applied DC field with two relaxation channels. Given the above this organic-inorganic hybrid can be consider as a rare example of multifunctional materials which exhibit dielectric, and magnetic activity.

Introduction

Organic–inorganic hybrid materials based on metallohalides (M = Co(II), Fe(II) Zn(II), Mn(II) Cu(II) etc.) form a large family of compounds exhibiting structural phase transition (PT). Diverse structures were found for these compounds, varying from zero-dimensional (0D) clusters, one-dimensional (1D) chains, two-dimensional (2D) layers to 3D frameworks. The structural diversity is caused mainly by the versatile metal-halide bonds and differing size and symmetry of the organic cations. Increased interest has been observed recently in metallohalide materials showing structural PTs, especially those exhibiting distinct dielectric anomalies. Crystal structures of 0D halidometallates(II) contain the discrete $[MX_4]^{2-}$ components. Despite their apparent structural simplicity, alkyl-ammonium and phosphonium/arsonium tetrahalidometallates of *d*-block and other metals ($[NR_4]^{n+}[MX_4]^{n-}$, where R = Me, Et, etc., X =

Cl, Br and $n = 1$ or 2) exhibit a rich diversity of ferromagnetic, ferroelectric, ferroelastic and incommensurate phases (Sawada *et al.*,[1] Shimizu *et al.*,[2] Styczeń *et al.*,[3,4] Zubillaga *et al.*,[5] Clay *et al.*,[6] Pressprich *et al.*[7]). Tetramethylammonium analogs have deserved special attention because these materials have become canonical models for studying disordered incommensurate–commensurate phase sequences (Lopez-Echarri *et al.*)[8]. It has turned out that for all materials in this class, the relationships between phases are conditioned by the orientations of component ions which undergo subtle changes with temperature (Barreda-Argueso *et al.*).[9]

In the case of halidocobaltate(II) hybrids, literature reports on organic-inorganic compounds exhibiting switchable dielectric properties are quite rare, except for tetraalkyl-ammonium and -phosphonium analogues. Most examples concern tetrahalidocobaltates(II) characterized by 0D structure with various polar cations *e.g.*; 3-chloro-2-hydroxypropyl trimethylammonium,[10] (H_2dabco-C_2H_5),[11] 1,4-diisopropyl-1,4-diazonia-bicyclo-[2.2.2]octane,[12] trimethylchloromethyl ammonium,[13] (*N*,*N*-dimethylbenzylammonium),[14] triethylbenzylammonium,[15] methyltriphenylphosphonium,[16] $[NH_2(C_2H_5)_2]$,[17] $[(CH_2)_7(NH_3)_2]$,[18] ethylammonium,[19] methylammonium.[20] Structural instability in these compounds is due to the dynamics of the organic cations. Ferroelectric properties within this type of compounds are unique. To the best of our knowledge, only three ferroelectrics have been synthesized so far; dimethylammonium analog – $[NH_2(CH_3)_2]_2CoCl_4$,[21] PT ($P2_1/n$ →polar) and *n*-dodecylammonium - $(C_{12}H_{25}NH_3)_2CoCl_4$,[22]. The most interesting appears to be an organic-inorganic hybrid (diisobutylammonium)$_3$ClCoCl$_4$, with a high Curie temperature of 372.5 K and significant spontaneous polarization of 4.6 $\mu C \cdot cm^{-2}$. This is the first example of a hybrid photosensitive ferroelectric that is strongly sensitive to specific wave band illumination.[23]

Recently, we have synthesized and characterized a novel cobaltate(II) organic-inorganic hybrid based on imidazolium cation - $(C_3N_2H_5)_2CoCl_4$ (**ICC**).[24] This compound was found to undergo two structural PTs: continuous at 245.5 K (from phase I to II) and a discontinuous one at 234/237 K (cooling/heating) (II→ III). **ICC** crystallizes in the monoclinic space groups $C2/c$ and $P2_1/c$ in phase (I) and (III), respectively. The intermediate phase (II) appeared to be incommensurately modulated. The dielectric spectroscopy and proton magnetic resonance (^{1}H NMR) studies showed that dynamics of imidazolium cations contributes mainly to the PTs mechanism in **ICC**. Additionally, this analog revealed weak antiferromagnetic properties. In recent literature reports, pyrrolidine appears more and more often as a cation with a permanent dipole moment in organic-inorganic hybrids, which is associated with large possibilities of reorientation of the cation in the crystal lattice.[24–29] This probability increases the chance of phase changes and, consequently, promising physicochemical properties. Among the compounds, one can distinguish a group containing metals M^{2+}: for example pyrrolidinium trichloridocuprate $(C_4NH_{10})CuCl_3$, which crystallizes in α and β forms in *C*2/*c* space group.[30,31] Studies with a more broad spectrum were carried out for pyrrolidinium derivatives based on Mn(II): $(C_4NH_{10})MnCl_3$ and $(C_4NH_{10})MnBr_3$, which additionally exhibit luminescence properties.[32,33] Moreover, it should be noted that both compounds are ferroelectrics, and the bromide derivative also exhibits ferromagnetic properties. Recently, we have synthesized and characterized two pyrrolidinium analogs based on Sb(III); $(C_4NH_{10})_3[Sb_2Cl_9]$[25] and $(C_4NH_{10})_2[SbCl_5]$.[34] In all pyrrolidinium halogenometallate hybrids dynamics of cations plays a key role in the mechanism of PTs.

Halidocobaltate(II) hybrids can be also obvious leaders in the field of magnetic materials due to their ability to construct SIMs materials that exhibit slow magnetization relaxation, which may have potential applications in high-density information storage, spintronics and quantum processing. Experimental and theoretical calculations suggest that a high-spin Co(II) ion, which may exhibit large magnetic anisotropy with a flexible zero field splitting parameter with both an easy-axis ($D<0$) and an easy-plane anisotropy ($D>0$) depending on its coordination geometry and the distortion degree of its surroundings, is an excellent candidate for building SIMs.[35,36] In this respect, examples of SIMs with this metal ion include trigonal planar,[37] tetrahedral,[38,39] square-pyramidal,[40,41] trigonal bipyramidal,[42] octahedral,[43] pentagonal bipyramidal,[44] and square antiprism[45] mononuclear complexes as well as a few coordination polymers containing six-coordinate cobalt(II) ions.[46]

Special attention, for example, has been paid to establishing a magneto-structural correlation based on D for low-coordinated tetrahedral Co(II) mononuclear compounds, for which the magnetic anisotropy can be considerably influenced not only by the variations in the first and second coordination spheres but also by the type of terminal ligand and the nature of metal–ligand covalent bonding.[47-49] In particular, it has been shown that heavier and softer terminal ligands are able to modify significantly the anisotropy of Co(II) centers.[50,51] The breakthrough work of this area was example of a homoleptic mononuclear compound $[PPh_4]_2[Co(SPh)_4]$ reported by Zadrozny et al., which possess a large negative ZFS parameter D, $-70\ cm^{-1}$, and exhibit SIM behaviour in a zero static magnetic field.[50] So, combination of the functional properties of both ingredients (organic and inorganic) makes this field of research very attractive.

In search for new non-centrosymmetric cobaltate(II) organic–inorganic hybrids we have embedded in the crystal structure unsymmetrical pyrrolidinium cations. Herein, in the process of designing new switchable dielectric PT materials, we synthesized two 0D organic-inorganic hybrid compounds based on Co(II); $(C_4NH_{10})_2CoCl_4$ (**PCC**) and $(C_4NH_{10})_2CoBr_4$ (**PCB**), which exhibit complex sequence of PTs. Moreover, cation dynamics gives rise to the interesting dielectric properties. The molecular motions of pyrrolidinium cations have been studied by means of relaxation measurements in the proton magnetic resonance (^{1}H NMR). Magnetic properties of mononuclear Co(II) complexes were also studied. The results obtained in this work suggest new pathways for further research on ferroic materials based on cobalt-chloride/bromide hybrid organic-inorganic derivatives.

Experimental

Synthesis:

All reagents in the synthesis were of reagent grade purity and were used as commercially obtained.

$[C_4H_{10}N]_2CoBr_4$ (**PCB**) crystals were prepared by the reaction of cobalt(II) bromide ($CoBr_2$, Sigma-Aldrich 99%) dissolved in distilled water and pyrrolidine (C_4H_8NH, Sigma-Aldrich >99.5%) at molar ratio 1 : 1 in concentrated hydrobromic acid (HBr, Sigma-Aldrich 48%). The mixture was left to stand for several days. Needle-shaped blue crystal were grown.

$[C_4H_{10}N]_2CoCl_4$ (**PCC**) blue needle like crystals were obtained in a similar way ($CoCl_2$,Sigma-Aldrich 99%) and concentrated 36% HCl was used. Both of materials are highly hygroscopic. The results of the elemental analysis for C/N/H are close to theoretical ones (Table S1), and the experimental PXRD is well consistent with the corresponding simulated one indicating phase purity of two title compounds (Figure S1).

Thermal analysis

Differential Scanning Calorimetry (DSC) experiments were performed on a Perkin Elmer model 8500 differential scanning calorimeter calibrated using *n*-heptane and indium, under a nitrogen atmosphere in hermetically sealed Al pans on the polycrystalline material.

Simultaneous Thermogravimetric Analysis (TGA) and Differential Thermal Analysis (DTA) were performed on a Setaram SETSYS 16/18 instrument in the temperature range 300–900 K with a ramp rate 2 K min^{-1} (Figure S2). The scans were performed in flowing nitrogen (flow rate: 1 dm^3 h^{-1}).

X-ray analysis

Diffraction data for **PCB** and **PCC** crystals were collected on an Oxford Diffraction Xcalibur four-circle diffractometer with Mo Kα radiation (λ = 0.71073 Å) equipped with Atlas CCD detector (Section 3 in ESI). The collected diffraction data for all compounds were processed with the CrysAlis PRO program.[52] The structures were solved by direct methods using SHELXS or SHELXT programs and refined by least squares method on F^2 by SHELXL software with the following graphical user interfaces of OLEX.[53,54] Atomic displacements for non-hydrogen atoms were refined using an anisotropic model. All hydrogen atoms were placed in ideal positions and refined as riding atoms with relative isotropic displacement parameters. The crystal parameters, data collection and the refinement are summarized in Table S2. The crystallographic material can also be obtained from the CCDC (nos: 2082868-2082871).

Dielectric measurements

The complex dielectric permittivity, $\varepsilon^* = \varepsilon' - i\varepsilon''$, was measured with an Agilent E4980A Precision LCR Meter between 100 and 400 K in the frequency range between 135 Hz and 2 MHz. The overall error was less than 5%. The polycrystalline sample of **PCC** with about 16 mm^2 in area and 1.2 mm thickness and single crystal sample of **PCB** with about 6 mm^2 in area and 0.7 mm thickness were measured. Conductive silver paste was stuck on the opposite faces of materials and used as electrodes.

Optical Measurements

The ferroelastic domain structures of the **PCC** and **PCB** crystals were observed by means of an Olympus BX53 optical polarization microscope combined with a LINKAM THM-600 heating/cooling stage. The temperature was stabilized to within 0.1 K (more in Section 4 (ESI)).

Nuclear Magnetic Resonance

T_1 measurements were carried out as a function of temperature at 25 MHz using an ELLAB TEL-Atomic PS 15 spectrometer. Inversion recovery pulse sequence was used. The temperature of the sample was varied from 83 to 420 K using an UNIPAN 660 temperature controller operating on Pt 100 sensor providing long time temperature stability better than 1 K. Single exponential magnetization decays were observed in the whole temperature range. The estimated average error of the measured T_1 values is 5%.

The second moment (M_2) data of the ^{1}H NMR line was measured on a ELLAB CW continuous wave spectrometer at the resonance frequency of 26.8 MHz. The second moment values were calculated by numeral integration of the first derivative of an absorption line and corrected for the finite modulation amplitude (more in Section 5 (ESI)).

EPR and Far-Infrared Magnetic Spectroscopy (FIRMS) studies

The high–field, high–frequency EPR spectra at temperatures ranging from *ca*. 3 K to 290 K were recorded on a home–built spectrometer at the EMR facility of the National High Magnetic Field Laboratory (NHMFL). The instrument is equipped with a superconducting magnet (Oxford Instruments) capable of reaching a field of 17 T. Microwave frequencies over the range 52–630 GHz were generated by a phase–locked Virginia Diodes source, producing a base frequency of 8–18 GHz, which was multiplied by a cascade of frequency multipliers. The instrument is a transmission–type device and uses no resonance cavity. Far Infrared Magnetic Spectroscopy was performed at the NHMFL on a 17 T vertical-bore superconducting magnet using a Fourier-transform infrared spectrometer Bruker Vertex 80v. The evacuated (~4 mBar) optical beamline was used for their coupling and the experimental set-up was equipped by a mercury lamp and a composite silicon bolometer (Infrared Laboratories), as a THz radiation source and detector, respectively. Eicosane pellets containing the studied compound were measured in the spectral region between 18 and 730 cm^{-1} (0.55-22 THz) with the resolution of 0.3 cm^{-1} (9 GHz). Both sample and bolometer were cooled by a low-pressure helium gas to the temperature of 4.6 K. Transmittance spectra were calculated as the THz intensity spectrum at each magnetic field divided by the THz intensity spectrum averaged for all fields.

Magnetic data

The DC magnetic data was taken using the SQUID magnetometer (MPMS, Quantum Design) with *ca*. 22 mg of sample. The susceptibility data were acquired at the B_{DC} = 0.5 T between T = 1.8 and 300 K. This was corrected to the underlying diamagnetism and transformed to the effective magnetic moment. The magnetization data was taken at low temperatures T = 2.0 up to $B_{\max}$ = 5.0 T. No remnant magnetization has been detected. The AC susceptibility data were taken with the same apparatus and the same samples using the amplitude of the oscillating field B_{AC} = 0.3 mT. Three regimes were used: (*i*) scan of the AC susceptibility as a function of the field up to B_{DC} = 1 T at T = 2.0 K for a set of four trial frequencies *f*; (*ii*) scan of the AC susceptibility as a function of temperature for 22 frequencies of the oscillating field and a set of temperatures ranging between T = 1.8 and 7.0 (8.0) K, all performed at the properly selected field B_{DC} = 0.2 (0.15) T.

3. Results

3. 1 Thermal properties

DSC measurements (Figure 1) show the occurrence of one transformation above and below room temperature (RT). The transition between **I** and **II** is characterized by a small temperature hysteresis (1 K and 6 K, for **PCB** and **PCC** respectively), while the transition between **II** and **III** reveals a very large difference between the heating and cooling cycles: 46 K for **PCB** and 55 K for **PCC**.

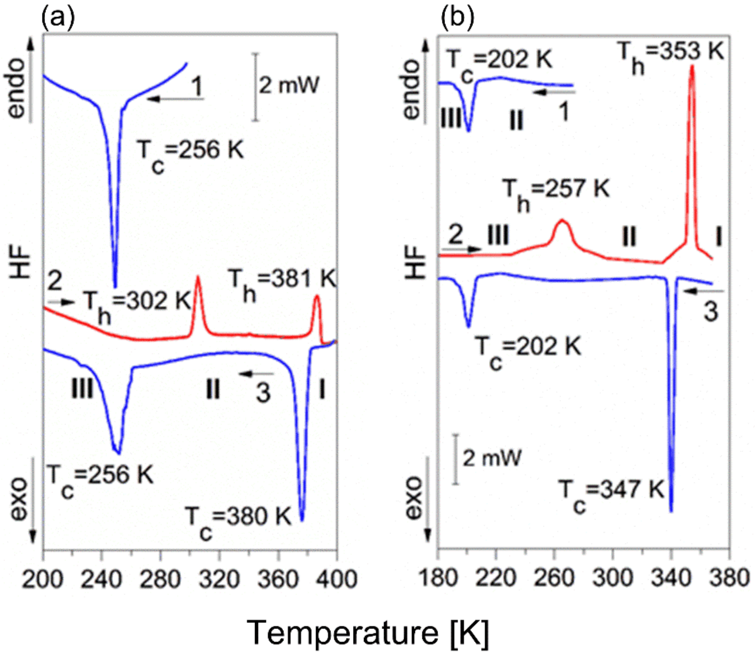

Figure 1. DSC curves for (a) **PCB** (m = 13.250 mg) and (b) **PCC** (m = 12.985 mg) during cooling and heating samples.

The transition entropy for the PTs in **PCB** are significant: $\Delta S_{(I\rightarrow II)}$ = 7 J·K^{-1}·mol^{-1} (380 K) and $\Delta S_{(II\rightarrow III)}$ = 10.0 J·K^{-1}·mol^{-1} (256 K). Both PTs are evidently first order and ΔS_{Tr} value proves an 'order-disorder' mechanism of these transitions. Quite similar phase situation occurs in the **PCC** compounds. The corresponding transition entropy values are: $\Delta S_{(I\rightarrow II)}$ =12 J·K^{-1}·mol^{-1} (347 K) and $\Delta S_{(II\rightarrow III)}$ = 6.5 J·K^{-1}·mol^{-1}. It should be noticed that total entropy changes for these two transitions for **PCB** and **PCC** are comparable (17 and 18.5 J·K^{-1}·mol^{-1}, respectively). The thermal stability of compounds determined by TGA/DTA measurement is 400 K for **PCC** and 515 K for **PCB** (Figure S2).

3.2 Crystal structures of ***PCC*** *and* ***PCB***

The room temperature phases of the title compounds, **PCC** and **PCB**, are not isomorphous (more in ESI (Part 3)). The chloride analogue crystallizes in the monoclinic $P2_1/c$ space group type with the monoclinic angle being very close to 90° (within the experimental error). The measured crystal demonstrated typical in this case twinning with the following twin matrix {-1 0 0 0 -1 0 0 0 1}. The independent part of the structure consists of four $[CoCl_4]^{2-}$ anions and eight $(C_4H_{10}N)^+$ cations ($Z' = 4$) (Figure 2(a)). The bromide analog crystallizes in the monoclinic $P2_1/n$ space group with only one $[CoBr_4]^{2-}$ anion and two $(C_4H_{10}N)^+$ cations ($Z' = 1$) in the independent part of the structure. The monoclinic angle deviates by ~3.7° from the right angle (Figure 2(b)).

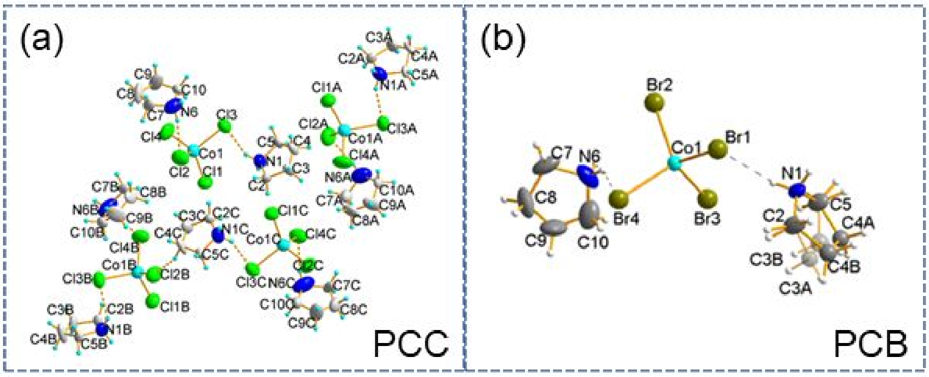

Figure 2. The asymmetric unit of (a) **PCC** and (b) **PCB** at RT. Displacement ellipsoids are shown at the 20% probability level.

One may notice the similarities in the crystal packing projections of room temperature phases of chloride and bromide analogues (Figure 3) as well as the relation between their cell parameters ($a_{\mathrm{Cl}} \approx 2 \cdot c_{\mathrm{Br}}$, $b_{\mathrm{Cl}} \approx a_{\mathrm{Br}}$, $c_{\mathrm{Cl}} \approx 2 \cdot b_{\mathrm{Br}}$, $V_{\mathrm{Cl}} \approx 4 \cdot V_{\mathrm{Br}}$). Both chloride and bromide analogs exhibit solid-to-solid state PTs above room temperature. Structural studies on both analogs' high temperature phases were undertaken, but due to considerable weakening of diffraction intensities they did not provide reliable results. Both analogs seem to crystallize in the similar orthorhombic cells in the high temperature region. The models of the high temperature phases' structures were proposed. The best fit was obtained for the refinement in $Pna2_1$ non-centrosymmetric space group with one $[CoX_4]^{2-}$ anion and two $(C_4H_{10}N)^+$ cations ($Z' = 1$) in the independent part of the structure for both chloride and bromide analogs. Thus, it may be stated that there is a common prototype high-symmetry phase for both analogs, which undergoes different deformations on cooling to room temperature.

PCC: $a_{RT} \approx 2 \cdot b_{HT}$, $b_{RT} \approx c_{HT}$, $c_{RT} \approx 2 \cdot a_{HT}$, $V_{RT} \approx 4 \cdot V_{HT}$

PCB: $a_{RT} \approx c_{HT}$, $b_{RT} \approx a_{HT}$, $c_{RT} \approx b_{HT}$, $V_{RT} \approx V_{HT}$

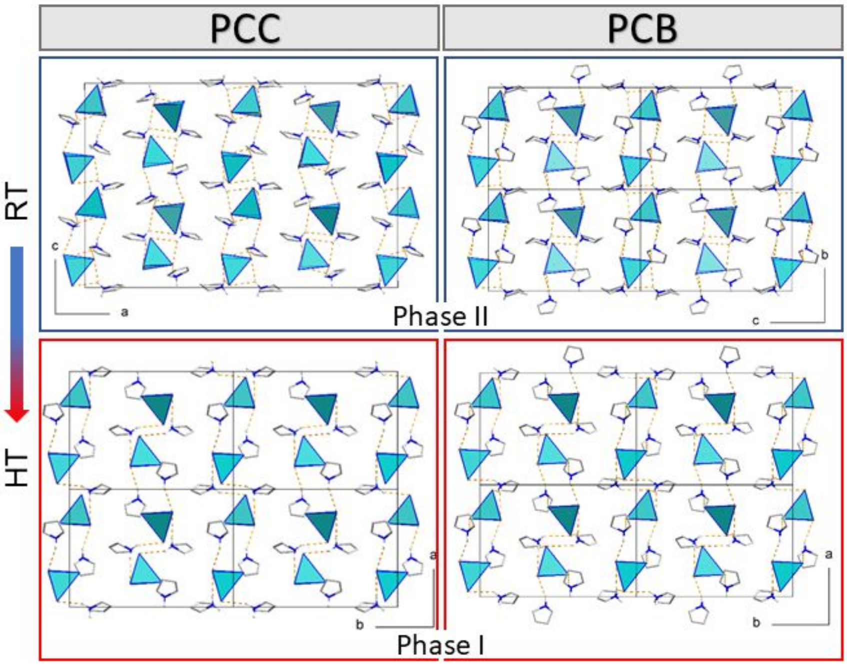

Figure 3. Projection of the crystal structure packing of phases **II** (RT) and **I** (HT) of **PCC** and **PCB** .

Crystal structure packing motif is common for both chloride and bromide analogs with the differences arising from different deformations that take place during the HT→RT PTs. In general, both RT phases are built from tetrahedral $[CoX_4]^{2-}$ anions and $(C_4H_{10}N)^+$ cations in 1:2 ratio. The cation atoms form 5-membered rings and are characterized by large thermal ellipsoids. The N atoms positions were arbitrary assigned to the atoms that possess the lowest thermal vibrations and produce the shortest donor-acceptor distances in the potential hydrogen bonds with halide anions. Each $(C_4H_{10}N)^+$ cation binds two neighbouring $[CoX_4]^{2-}$ anions through the formation of intermediate strength hydrogen bonds. Such type of bonding results in the formation of H-bonded layers, perpendicular to the *a*-axis direction in the chloride analog and columns, parallel to the *b*-axis direction, in bromide analog.

The mechanism of PT in both chloride and bromide analogs, which occur above-room temperature, involves mainly the reorientation of pyrrolidinium cations and the changes in their dynamic behaviour. The tetrahedra of $[CoX_4]^{2-}$ adjust themselves to the network of hydrogen bonds formed with amino-groups of cations and do not undergo considerable reorientations. In the RT phase of chloride analog four independent, but geometrically very similar $[CoCl_4]^{2-}$ tetrahedra are present.

3.3 Dielectric measurements

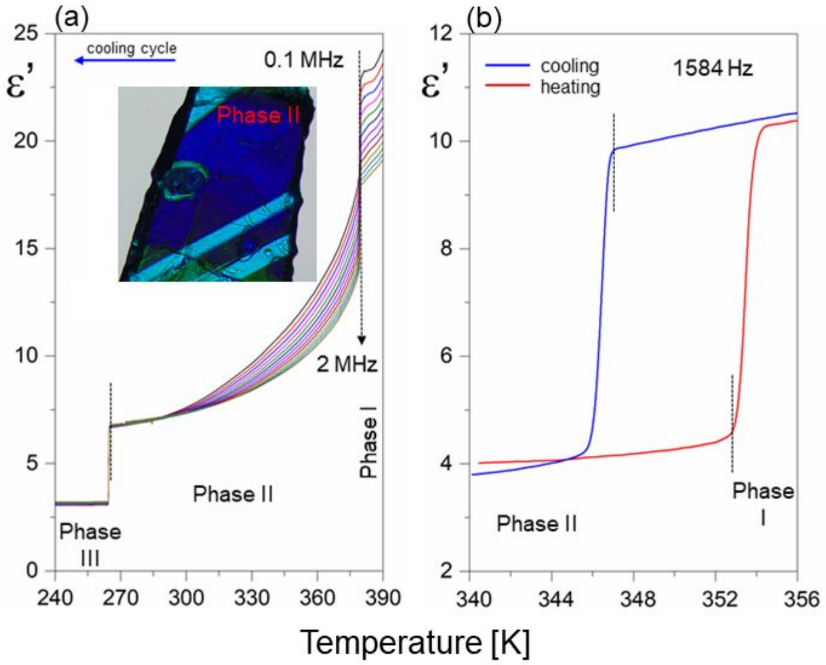

Figure 4. Frequency dependencies of real part of dielectric constant (ε') at various temperatures for (a) **PCB** during cooling at 0.1 MHz; (b) **PCC** during heating and cooling at 1584 Hz.

The dielectric response (Figure 4) confirmed the sequence of the PTs recorded in the calorimetric measurements for **PCA** and **PCB**. The temperature dependence of the real part of the complex electric permittivity in the frequency range 0.1 – 2 MHz for **PCB** (powdered sample) during cooling cycle is shown in Figure 4(a). It is clearly seen that **PCB** undergoes two PTs at 380 and 256 K which are accompanied by the rapid decrease in the ε' with Δε'≈4-5 and Δε'≈3, respectively. The PT (**II→III**) leads to a drastic breaking of the single crystal sample thus the measurements were carried out only during cooling. The insert in Figure 4(a) shows the ferroelastic domain structure which was induced during the PT (**I→II**). A detailed description of the ferroelastic domains is presented in the ESI (Section 4 (ESI) – Optical Properties). In the case of **PCC** the deformation of the sample through the lowest temperature PT (**II→III**) at 202 K is even more drastic than for **PCB** thus the dielectric response (ε'(T)) is illustrated only around ferroelastic transition (**I→II**) which is well reversible (Figure 4(b)). One can observe a distinct dielectric increment, Δε'≈ 6, measured at *ca.* 1.5 kHz. The low dielectric state (Phase **II**) represents 'switch off' and the high dielectric state (Phase **I**) indicates 'switch on' thus **PCC** is a good candidate for the temperature-induced dielectric switchable materials.

3.4 ^{1}H NMR Spin−Lattice Relaxation Times Studies

The temperature dependencies of the 25 MHz proton nuclear relaxation times (T_1) for **PCC** and **PCB** are shown in Figure 5. Both temperature dependencies of T_1 are comparable and values of T_1 are progressively growing from a fraction of a millisecond to more than three milliseconds. The T_1 values measured for **PCC** at high temperatures are about half as high as those for **PCB**, while the low-temperature data for both compounds are similar. It should be noted that such short times (typical ranges of T_1 are from milliseconds to seconds) are the result of the presence of ^{59}Co atoms possessing unpaired electrons.

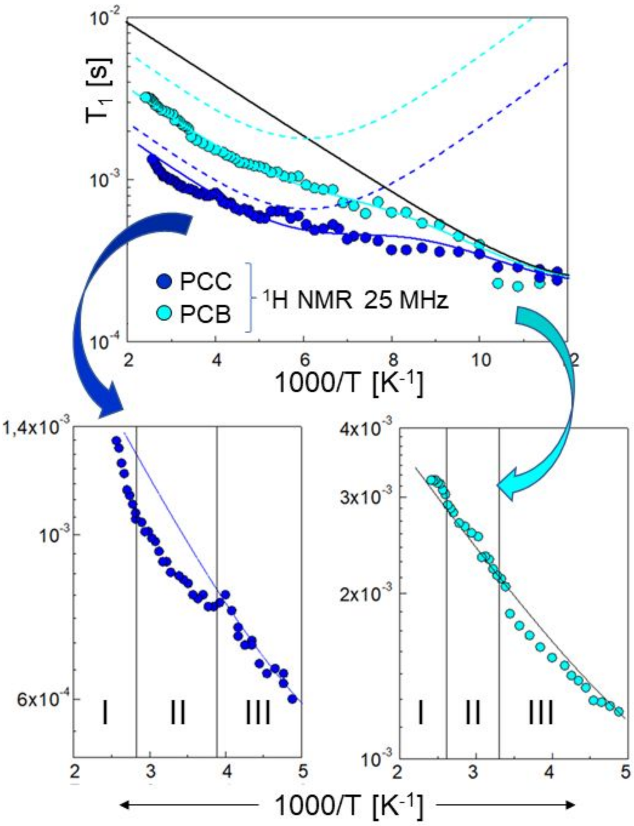

Figure 5. ^{1}H spin–lattice relaxation time T_1 versus temperature for **PCB** (cyan points) and **PCC** (blue points) at 25 MHz and theoretical completely fit (solid lines) and components (dotted lines) obtained as a sum of two relaxation processes (eq. (4)).

^{1}H spin−lattice relaxation time in the studied compounds consists of two contributions: the first one, ^{1}H −^{1}H, results from the dipole−dipole interactions between protons of the pyrrolidinium cations and the second one, the ^{1}H − ^{59}Co relaxation pathway, results from the dipole−dipole couplings of protons with the unpaired electron spin of ^{59}Co.[22,24,28,34,55-57]

$$\frac{1}{T_1}=\frac{1}{T_{1\,HH}}+\frac{1}{T_{1\,HCo}}=C_{HCo}\left[3J(\omega_H)+7J(2\omega_S)\right]+C_{HH}\left[J(\omega_H)+4J(2\omega_H)\right] \qquad \text{(eq. 1)}$$

where the J(ω) are spectral density functions being Fourier transform of time correlation functions describing the stochastic fluctuations of the dipole−dipole interaction. The spectral densities taken at ω_H and ω_S are associated with different correlation times, $\tau_{eff,1}$ and $\tau_{eff,2}$, respectively, defined as $\tau_{eff,1}^{-1} = \tau_c^{-1} + 1/T_{1,e}$ and $\tau_{eff,2}^{-1} = \tau_c^{-1} + 1/T_{2,e}$,where $T_{1,e}$ and $T_{2,e}$ are electron spin−lattice and electron spin−spin relaxation rates, respectively.[22,24,28,34,55-57] C_{HH} and C_{HCo} are relaxation dipole−dipole constants. The C_{HCo} relaxation constant is defined as:

$$C_{HCo} = \frac{2}{15} S(S+1) \left(\frac{\mu_0}{4\pi} \frac{\gamma_H \gamma_S \hbar}{r_{HCo}^3} \right)^2 \qquad \text{(eq. 2)}$$

where r_{HCo} is an effective inter atomic distance, γ_H is proton gyromagnetic ratio and γ_s is the electron gyromagnetic ratio, S is the electron spin quantum number for Co(II) S = 3/2. As $\gamma_S/\gamma_H \cong 650$ the relaxation constants C_{HCo} and C_{HH} become comparable for $r_{HCo} \cong 8r_{HH}$. The T_{1HCo} contribution dominates, when r_{HCo} is smaller. As we noted above, the significantly shorter spin-lattice times T_1 for **PCC** and **PCB** measured here confirm that the observed relaxation is mostly due to the ^1H −^{59}Co dipole−dipole interactions and ^1H −^1H may be neglected. On the other hand, when we compare contribution of both spectral density function $J(\omega_S)$ and $J(\omega_H)$ to overall relaxation we may conclude that the contribution associated with $J(\omega_S)$ can be neglected as well, since $\omega_S \tau_c >> 1$. As a result, we obtain the simplified expression for the ^1H spin−lattice relaxation time

$$\frac{1}{T_1} = 3C_{HCo} J(\omega_H) = K_1 \frac{\tau_{c,1}}{1+\omega_H^2 \tau_{c,1}^2} \qquad \text{(eq. 3)}$$

This equation takes into account the fact that the correlation time τ_c is shorter than $T_{1,e}$ and usually $\tau_{eff,1} \cong \tau_{c,1}$. A cursory analysis of measured relaxation times T_1 versus temperature for **PCC** and **PCB** samples leads us to conclusion that the observed dependencies require at least two relaxation mechanisms:

$$\frac{1}{T_1} = K_1 \frac{\tau_{c,1}}{1+\omega_H^2 \tau_{c,1}^2} + K_2 \frac{\tau_{c,2}}{1+4\omega_S^2 \tau_{c,2}^2} \qquad \text{(eq. 4)}$$

In Figure 5 are drawn the theoretical temperature dependencies of the relaxation time fitted using the above equation (see also Table S11). As it is visible in Figure 5 the theoretical line for **PCB** quite accurately coincides with the experimental data. In the case of **PCC**, the dynamical parameters are the same except the constant K_1, which is nearly three times smaller than that one of **PCB**. It means that the low temperature relaxation process for both compounds is practically the same and the relaxation process due to the $^1H - ^{59}Co$ dipole−dipole interactions at high temperatures is more sensitive to the physical properties of the sample. In case of **PCC** the fit line matches the experimental points rather roughly, mainly due to the presence of several PTs. A conclusion from the T_1 measurements is that the lowest temperature transitions (**II→III**) are the most sensitive to PT in both compounds. The visible anomalies confirmed the main role of the pyrrolidinium cations dynamics in the PT mechanisms. The results of the M_2 measurements and discussion of possible motional state of cations with temperature for **PCC** and **PCB** are presented in ESI (Part 4).

We can briefly compare the basic features of the compounds under investigations. Both materials exhibit two reversible PTs connected with the dynamics of pyrrolidinium cations. **PCC** and **PCB** are isomorphous in the paraelastic/ferroelastic phases, however in their intermediate phases (**II**) they differ somewhat from a structural point of view.

The crystal structure packing theme is common to both chloride and bromide analogs. Phase **II** is composed of tetrahedral anions $[CoX_4]^{2-}$ and cations $(C_4H_{10}N)^+$ in the ratio 1:2. The organic subnetwork consists of 5-membered pyrrolidine rings which are characterized by a significant dynamic disorder. A pseudo-one-dimensional structure is formed as a chain in which the $[CoX_4]^{2-}$ tetrahedra are bridged by pyrrolidinium cations via a hydrogen bond system. High-temperature PF (**II→I**) leads to an even greater disorder of the cations, while the positions of the $[CoX_4]^{2-}$ tetrahedra do not show significant changes in positions. There is a common high symmetry (orthorhombic) prototype phase for both analogs, which undergoes different deformations when cooled to room temperature, resulting in differentiation of unit cell parameters. Significant entropy factors are consistent with the structural picture that indicates significant changes in cation dynamics at the PT points for both compounds. Accordingly, all observed PTs are described by ‘order-disorder’ mechanisms. X-ray studies have shown that PT (**II↔I**) is accompanied by a change in the crystallographic system, and therefore these transformations belong to the class of ferroic transformations (2/mFmm2), according to the Aizu classification, accompanied by the induction of ferroelasticity. This image is consistent with the observation of crystals under a polarizing microscope for which the ferroelastic domain structures in phase **II** were observed for **PCC** and **PCB**. The proposed PT mechanisms were also confirmed by ^{1}H NMR studies. PT (**III→II**) turned out to be particularly active in both **PCC** and **PCB**, accompanied by clear anomalies in the T_1 versus 1/T characteristics. This proves that the change in the dynamic state of cations plays a key role in the mechanisms of low-temperature transitions. In turn, over phase **I** in **PCC** and **PCB** the pyrrolidine cations can perform twisted-envelope changes, and even rotations around the pseudo-five-fold axis of symmetry of the pyrrolidine ring.

3.5 Far-infrared magnetic spectroscopy

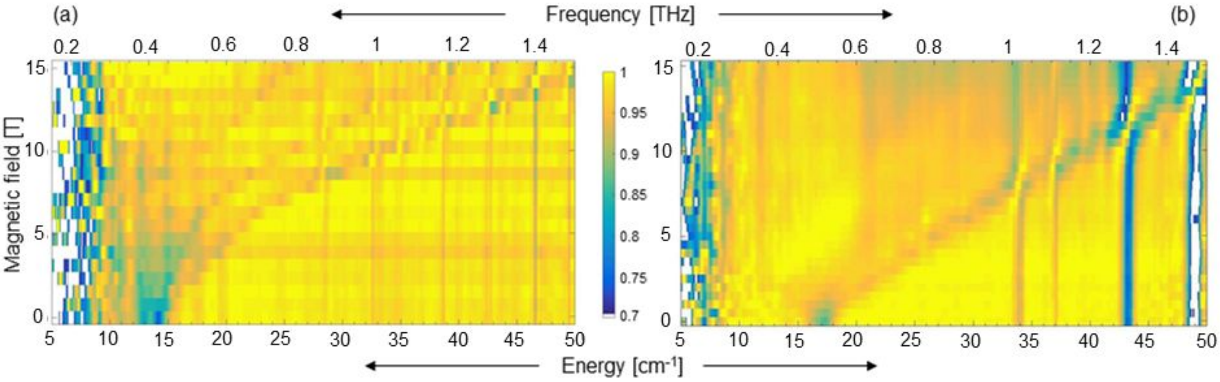

Figure 6. (a) A color map of FIRMS resonances observed for **PCC** at 5 K showing a zero-field transitions centered at 13-15 cm^{-1} evolving into powder patterns with an applied magnetic field. The tendency toward the blue color means the absorbance increases, whereas the yellow color corresponds to the transparent regions. The width of the zero-field transition is probably associated with the presence of 4 slightly different Co moieties (see Figure 2); (b) A color map of FIRMS resonances observed for **PCB** at 5 K showing a zero-field transition at 17 cm^{-1} evolving into powder patterns with an applied magnetic field. Zero-field spectral features at 34, 37, 43 and 50 cm^{-1} correspond to the phonon (vibrational) modes, which are nominally field-independent until they anti-crosses with the field-dependent transition at 17 cm^{-1}. The small shift of the phonon peaks with the applied magnetic field is a spectral manifestation of the spin-phonon coupling.

The EPR spectra of both compounds were of low quality revealing presence of contamination with the spin Hamiltonian parameters substantially different from those of the main species seen in FIRMS (Figure 6). In addition, the presence of four slightly different cobalt moieties in **PCC** apparently produces a set of spectra with slightly different parameters, making a precise simulation impossible. Large number of spectra were recorded with various microwave frequencies and the resonance fields were plotted as a function of frequency. In each case, zero-field resonances were found at frequencies consistent with those seen in FIRMS (Figure 6). The FIRMS transitions, whose frequency does not change with the magnetic field (like those at 34, 37, 43 and 50 cm^{-1} in Figure 6(b)), correspond to the phonon (vibrational) modes. Transitions observed at ~14 cm^{-1} in Figure 6(a) and at 17 cm^{-1} in Figure 6(b) are dependent on the magnetic field and therefore they are the magnetic transitions occurring between the ±1/2 and ±3/2 Kramers doublets. The frequency of these transitions at zero magnetic field is equal to the 'zero-field splitting' between the Kramers doublets and is related to the D and E parameters by $2\sqrt{D^2 + 3E^2}$.

The field-frequency dependencies reveal that both complexes exhibit large D, E parameters 7.8 and 2.1 cm^{-1}, respectively in **PCB** and 6.3, 1.3 cm^{-1}, respectively in **PCC** (Figure S14). Although these D and E values produce correct zero-field frequencies, they must be treated as estimations due to low spectra quality.

3.6 Magnetic studies - DC susceptibility

Magnetic data was acquired with the help of the SQUID magnetometer (MPMS, Quantum Design) at the applied field of B_0 = 0.5 T and, after correction to the underlying diamagnetism, transformed to the temperature dependence of the effective magnetic moment. Assuming g = 2.0, the expected high-temperature value for S = 3/2 spin system is $\mu_{\mathrm{eff}} = g[S(S+1)]^{1/2} = 3.87$ μ_{B}. The experimental data for **PCC** show a value of $\mu_{\mathrm{eff}} = 4.53$ μ_{B} at T = 300 K that implies $g > 2$ (Figure 7). This value is almost constant on cooling down to 7 K and then it drops down owing to a zero-field splitting. The magnetization data at T = 2.0 and B_{DC} = 5.0 T saturates to $M_1 = M_{\mathrm{mol}}/(N_{\mathrm{A}}\mu_{\mathrm{B}}) = 2.66$ which again confirms some zero-field splitting.

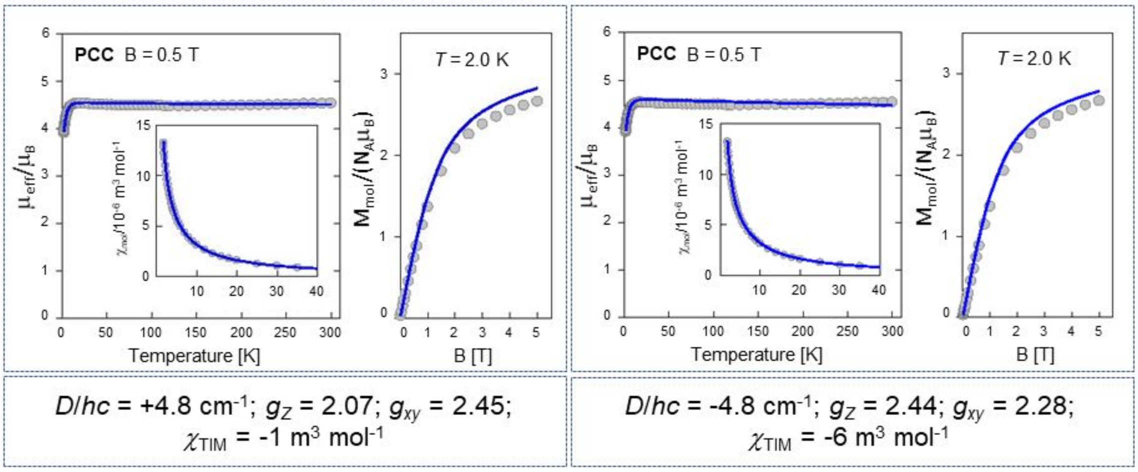

Figure 7. Left – temperature evolution of the effective magnetic moment (inset: molar magnetic susceptibility in SI units) for **PCC**; right – field dependence of the magnetization per formula unit. Lines – fitted.

In fitting the magnetic data, the standard model of the zero-field splitting has been employed with the spin Hamiltonian (eq. 5):

$$\hat{H}_k = D(\hat{S}_z^2 - \vec{S}^2/3)\hbar^{-2} + B\mu_{\mathrm{B}}(g_z \cos\vartheta_k + g_{xy}\sin\vartheta_k)\hbar^{-1} \qquad \text{(eq. 5)}$$

where *k* denotes grids distributed uniformly over the meridian (usually 16 grids) and ϑ_k is the polar angle. The eigenvalues enter the formulae of the statistical thermodynamics for the magnetic susceptibility and magnetization; their mean values mimic the powder average.[58] An involvement of the rhombic zero-field splitting parameter *E* is probably a too ambitious task due to over parametrization.

Both susceptibility and magnetization data with equal weights formed the error functional and its minimization gave the following set of magnetic parameters for **PCC**: $D/hc = +4.8$ cm^{-1}, $g_z = 2.07$, $g_{xy} = 2.45$; the additional correction refers to the temperature-independent magnetism $\chi_{\mathrm{TIM}} = -1$ m^3 mol^{-1} (it compensates uncertainties in the applied susceptibility corrections); the discrepancy factors for susceptibility and magnetization are $R(\chi) = 0.0063$ and $R(M) = 0.069$. The magnetic data can be fitted also with a reduced set $g_z = g_{xy}$ but then the reproduction of the magnetization is a bit worse. The sign reversal of *D* produces almost the same set of parameters, but values of g_{xy} and g_z are interchanged in order $D = \lambda(g_z - g_{xy})/2$ is fulfilled; the spin-orbit splitting parameter $\lambda/hc = -172$ cm^{-1} for Co(II).

The magnetic data for **PCB** are presented in Figure 8. It can be seen that the fitting procedure gave $D/hc = +7.0$ cm^{-1}, $g_z = 2.28$, $g_{xy} = 2.35$, $\chi_{\mathrm{TIM}} = 4.9$ m^3 mol^{-1}, and the molecular-field correction $zj/hc = -0.06$ cm^{-1}; $R(\chi) = 0.0075$ and $R(M) = 0.066$.

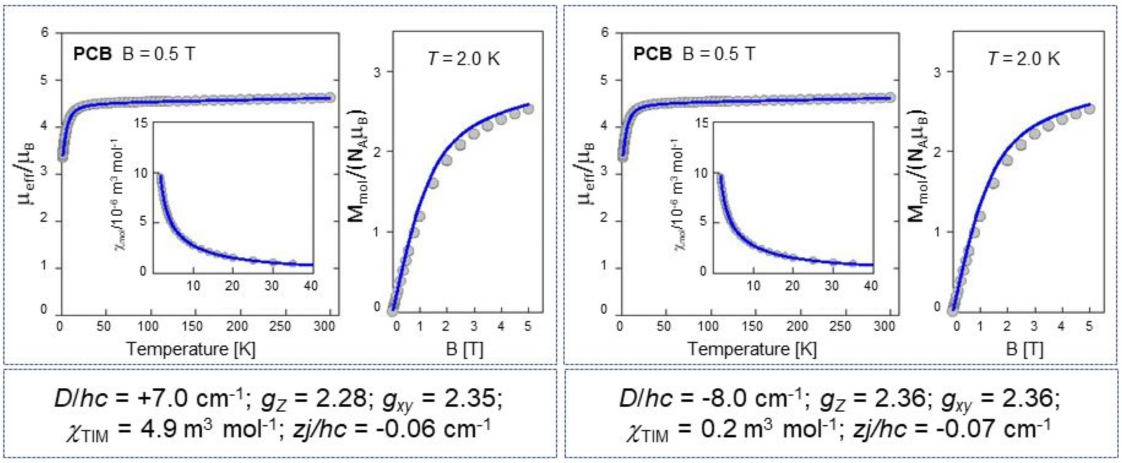

$D/hc = +7.0$ cm^{-1}; $g_Z = 2.28$; $g_{xy} = 2.35$;
$\chi_{\mathrm{TIM}} = 4.9$ m^3 mol^{-1}; $zj/hc = -0.06$ cm^{-1}

$D/hc = -8.0$ cm^{-1}; $g_Z = 2.36$; $g_{xy} = 2.36$;
$\chi_{\mathrm{TIM}} = 0.2$ m^3 mol^{-1}; $zj/hc = -0.07$ cm^{-1}

Figure 8. Left – temperature evolution of the effective magnetic moment (inset: molar magnetic susceptibility in SI units) for **PCB**; right – field dependence of the magnetization per formula unit. Lines – fitted.

In order to estimate the sign of the D-parameter in tetracoordinate Co(II) complexes a detailed inspection to the X-ray structure is helpful. Theoretical modelling using the generalized crystal field theory predicts that for the elongated tetrahedron (prolate disphenoid) of D_{2d}

symmetry (two angles << 109 deg) the D-parameter is negative. On the contrary, for a flattened tetrahedron (oblate disphenoid) of D_{2d} symmetry (two angles >> 109 deg) $D > 0$ holds true. **PCB** shows only a slight distortion from the tetrahedral geometry as Co-Br bond lengths are 2.395, 2.390, 2.386, and 2.393 Å. There are two bond angles Br-Co-Br ~ 111° which refers to a flattened tetrahedron for which $D > 0$ is predicted. The X-ray structure of **PCC** contains four different $[CoCl_4]^{2-}$ units and in all of them only two bond angles Cl-Co-Cl ~ 113°; this fact again leads to a prediction of the positive D.

AC susceptibility

AC susceptibility data was acquired first at T = 2.0 K for a set of representative frequencies of the alternating field (f = 1.0, 11, 111, and 900 Hz) by ramping the magnetic field from zero to B_{DC} = 1.0 T; the working amplitude B_{AC} = 0.3 mT was used. Representative data for the complex **PCC** is displayed in Figure 9. There is no absorption signal for both complexes (out-of-phase susceptibility component χ'') at the zero field owing to a fast magnetic tunneling. With the increasing external field, this component for **PCC** rises, passes through a maximum, and then attenuates; such a behavior confirms that the complex **PCC** exhibits a field supported slow magnetic relaxation. The position of the maximum, however, visibly depends upon the frequency *f* of the oscillating field.

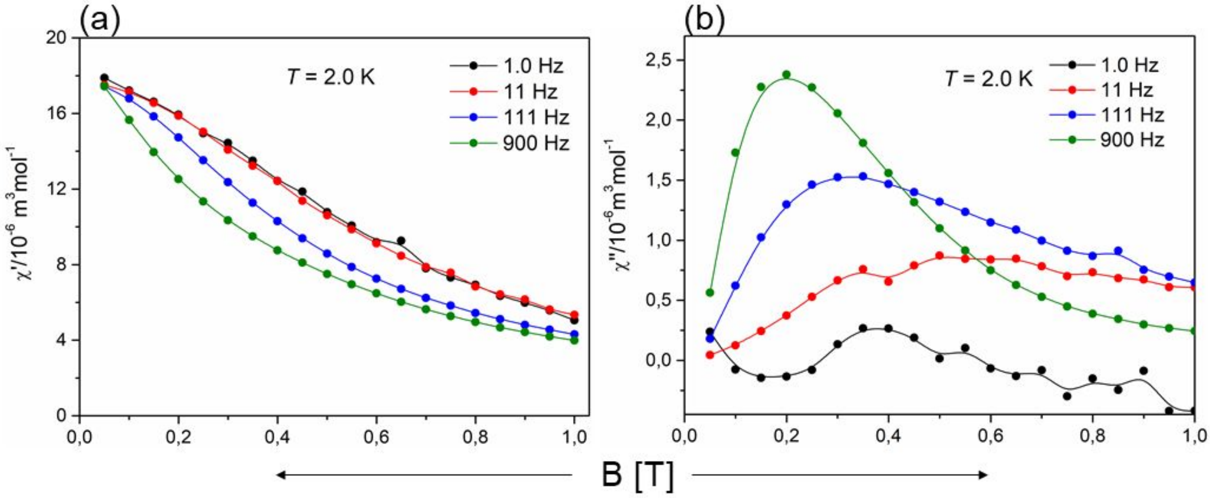

Figure 9. Field dependence of the AC susceptibility components for **PCC** at $T = 2.0$ K for a set of frequencies of the AC field. Lines serve as guide for eyes.

Subsequent experiments for **PCC** has been taken with the amplitude B_{AC} = 0.3 mT and the fixed external magnetic B_{DC} = 0.2 T (at which there is a maximum of the high-frequency signal) for a set of frequencies of the oscillating field ranging between *f* = 0.1 – 1500 Hz (Figure 10). A dominating peak is seen at the out-of-phase susceptibility χ" at frequencies *f* > 300 Hz. The peak position determines the relaxation time $\tau = 1/(2\pi f_{\mathrm{max}})$ that is τ(HF) = 324 μs at T = 1.8 K. On heating this peak moves to higher frequencies so that the high-frequency relaxation time decreases as shown in Table S12; numerical data were obtained through the fitting to the extended two-set Debye model. There is an on-set of the low-frequency (LF) relaxation channel seen as a minor peak at χ" *vs f* graph. The extracted relaxation time enters the Arrhenius-like plot as shown in Figure 11. The shift of the χ" peak above the frequencies limited by the used hardware does not allow applying the high-temperature extrapolation to the traditional Orbach-process equation in order to get barrier to spin reversal U_{eff} and the extrapolated relaxation time τ_0. To this end, the complex **PCC** at low temperature shows a field supported slow magnetic relaxation as a prerequisite of the single-ion magnetism.

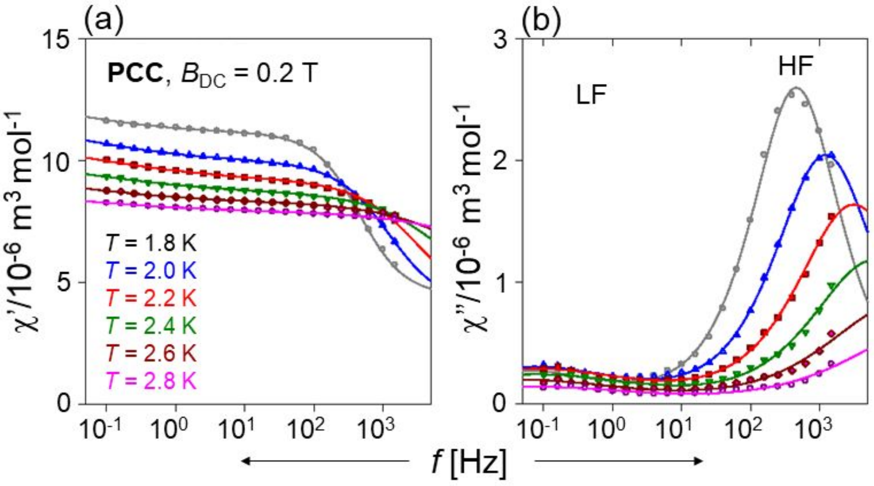

Figure 10. Frequency dependence of the AC susceptibility components for **PCC** at B_{DC} = 0.2 T. Lines – fitted by the two-set Debye model.

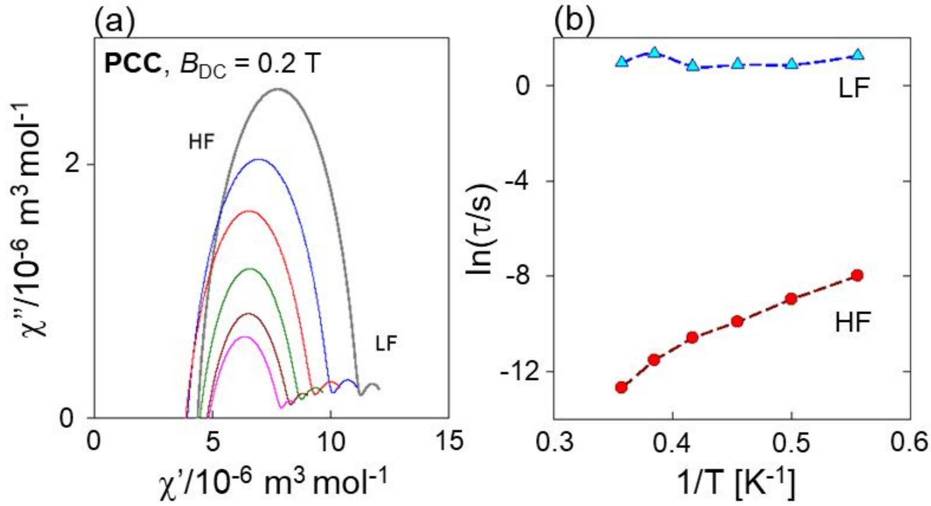

Figure 11. Argand plot (left) and the Arrhenius-like plot (right) for **PCC**.

Slow magnetic relaxation involving single or manifold relaxation processes has been found in numerous heptacoordinate, hexacoordinate, pentacoordinate, tetracoordinate and tricoordinate Co(II) complexes reported in recent years, although most of them exhibit magnetic relaxation only in applied external magnetic field.[59-64] One of the ultimate demand to observe this behavior is the presence of a large magnetic anisotropy, which generates an energy barrier for spin reversal, therefore many works are aimed at finding the principles of its controlled modification On the basis of this works it has been proved that the magnetic anisotropy of Co(II) complexes can be considerably influenced not only by the geometry of the coordination sphere but also by the type of terminal ligand and the nature of metal–ligand covalent bonding.[65-71] In particular for high-spin Co(II) tetracoordinate complexes with tetrahedral geometry it has been shown that softer terminal ligands such as sulfur, oxygen are able to modify significantly the anisotropy of such metal center.[50] Our study reveal that also other ligands such as halides holds the key to altering the magnitude and sign of the D value of complexes. The observation of positive D value for both complexes is quite different from earlier prediction in literature.[70] However Vaidya at all[71] present an examples of series of mononuclear tetrahedral Co^{II} complexes with a general molecular formula $[CoL_2X_2]$ [L=thiourea and X=Cl, Br, I] with the same sign but higher magnitude of the magnetic anisotropy for chloride and bromide analogs. This study reveals that heavier ligating atoms (such iodide) with large spin–orbit coupling enhance the metal–ligand covalency, which tends to stabilize easy-axis magnetic anisotropy in contrary to smaller metal–ligand covalency of the Co-Cl and Co-Br bonds stabilize easy-planes magnetic anisotropy in tetrahedral Co^{II} complexes. Higher value of D in **PCB** than **PCC** confirm this hypothesis. The smaller magnitude of D in our complexes can be the results of only a slight distortion from the tetrahedral geometry realized by the similar four $Co-X$ bonds. Also, we rationalize that the absence of slow magnetic relaxation behavior in **PCC** and **PCB** under zero external magnetic field is due to the lack of a pure ground state in both complexes, and further the large E/D value effectively triggers QTM rather than a thermally assisted Orbach process.

Conclusions

Single crystals of two organic-inorganic hybrids based on pyrrolidinium-tetrahalidocobaltates were successfully synthesized. They have 0D structures with isolated $[CoCl_4]^{2-}$ tetrahedra separated by disordered pyrrolidinium cations. A stepwise ordering of organic cations cations leads to two PTs **PCC** at 347/353 K (**I** ↔ **II**) and 202/257 K (**II** ↔ **III**) whereas **PCB** at 380/381

K (**I** ↔**II**) and 256/302 K (**II** ↔ **III**). Optical observations in the polarized light and single crystal X-ray diffraction measurements revealed that for both compounds the ferroic PT (**I**→**II**) belongs to the ferroelastic species mm2F2/m in the Aizu notation. This work confirms the assumption that introducing a mobile organic cations into tetrahalidocobaltates network might construct compounds with multiple properties. The DC magnetic data shows a magnetic anisotropy, which was confirmed by high-field HF EPR measurement together with FIRMS method due to determine the exact large D value for **PCC** (4.80 cm^{-1}) and **PCB** (7.00 cm^{-1}). The AC susceptibility data confirms that only complex **PCC** exhibit a slow magnetic relaxation under small applied DC field with two relaxation modes. To generalize, surrounding a tetrahedral Co^{II} ion by heavier - donor ligands of similar p/s strength ought to stabilize easy-plane anisotropy with rather large E/D ratio.

Corresponding Author

*anna.piecha@chem.uni.wroc.pl (Anna Piecha-Bisiorek)

Author Contributions

The manuscript was written through contributions of all authors. All authors have given approval to the final version of the manuscript.

Acknowledgments

The magnetic measurements was supported by University of Wroclaw program IDUB (BPIDUB. 4610.17.2021.KP.B) (A.B.) The National High Magnetic Field Laboratory is supported by National Science Foundation Cooperative Agreement No. DMR-1644779 (A.O., M.O) Slovak grant agencies (APVV 16-0039, APVV 18-0016, VEGA 1/0919/17 and VEGA 1/0013/18) are acknowledged for the financial support.

References

1 S. Sawada, Y. Shiroishi and A. Yamamoto, *Ferroelectrics*, 1978, **21**, 413–414.

2 H. Shimizu, N. Kokubo, N. Yasuda and S. Fujimoto, *J. Phys. Soc. Japan*, 1980, **49**, 223–229.

3 E. Styczeń, A. Pattek-Janczyk, M. Gazda, W. K. Jóźwiak, D. Wyrzykowski and Z. Warnke, *Thermochim. Acta*, 2008, **480**, 30–34.

4 E. Styczeń, W. K. Jóźwiak, M. Gazda, D. Wyrzykowski and Z. Warnke, *J. Therm. Anal. Calorim.*, 2008, **91**, 979–984.

5 J. Zubillaga, A. Lopez-Eharri and M. J. Tello, *J. Phys. C Solid State Phys.*, 1988, **21**, 4417–4423.

6 R. Clay, J. Murray-Rust and P. Murray-Rust, *Acta Crystallogr.* 1975, **B31**, 289–292.

7 M. R. Pressprich, M. R. Bond and R. D. Willett, *Phys. Rev. B*, 1991, **43**, 13549–13558.

8 A. Lopez-Echarri, M. J. Tello, C. Socias and J. Herreros, *J. Phys. C Solid State Phys.*, 1985, **18**, 2631–2642.

9 J. A. Barreda-Argüeso, L. Nataf, Y. Rodríguez-Lazcano, F. Aguado, J. González, R. Valiente, F. Rodríguez, H. Wilhelm and A. P. Jephcoat, *Inorg. Chem.*, 2014, **53**, 10708–10715.

10 Y. Sui, Y. S. Zhong, W. T. Chen, G. X. Zhang, C. L. Liu and D. S. Liu, *J. Phys. Chem. C*, 2019, **123**, 14647–14651.

11 Q. Ji, L. Li, S. Deng, X. Cao and L. Chen, *Dalt. Trans.*, 2018, **47**, 5630–5638.

12 L. Z. Chen, D. D. Huang, Q. J. Pan and J. Z. Ge, *RSC Adv.*, 2015, **5**, 13488–13494.

13 X. N. Hua, C. R. Huang, J. X. Gao, Y. Lu, X. G. Chen and W. Q. Liao, *Dalt. Trans.*, 2018, **47**, 6218–6224.

14 F. Issaoui, W. Amamou, M. Bekri, F. Zouari, F. Dhahri and M. A. Valente, *J. Mol. Struct.*, 2019, **1189**, 175–180.

15 D. H. Wu and L. Jin, *Inorg. Chem. Commun.*, 2012, **23**, 98–102.

16 M. F. Mostafa, A. A. Youssef, T. S. El Dean, A. M. Mostafa and I. S. A. Farag, *Cryst. Res. Technol.*, 2008, **43**, 547–560.

17 V. Kapustianyk, S. Semak, M. Panasyuk, M. Rudko and V. Rudyk, *Phase Transitions*, 2019, **92**, 396–405.

18 M. F. Mostafa, S. S. El-khiyami and S. K. Alal, *J. Phys. Chem. Solids*, 2018, **118**, 6–13.

19 A. Sen, S. Roy, S. C. Peter, A. Paul, U. V. Waghmare and A. Sundaresan, *J. Solid State Chem.*, 2018, **258**, 431–440.

20 K. Horiuchi, *Phys. Status Solidi Appl. Res.*, 2004, **201**, 723–726.

21 V. E. Vasiliev, M. Rudiak, A. Bobrova and V. M. Varikash, *Tverd. Tela*, 1987, **29**, 1539.

22 M. M. Abdelkader and M. Abdelmohsen, *Mater. Res. Express*, 2019, **6**, 025608.

23 C. Ji, S. Liu, S. Han, K. Tao, Z. Sun, J. Luo, *Angew. Chem. Int. Ed.*, 2018, **57**, 16764-16767.

23 M. Kunitski, C. Riehn, V. V Matylitsky, P. Tarakeshwar and B. Brutschy, *Phys. Chem.*

Chem. Phys., 2010, **12**, 72–81.

24 A. Piecha-Bisiorek, A. Bieńko, R. Jakubas, R. Boča, M. Weselski, V. Kinzhybalo, A. Pietraszko, M. Wojciechowska, W. Medycki and D. Kruk, *J. Phys. Chem. A*, 2016, **120**, 2014–2021.

25 M. Wojciechowska, A. Gągor, A. Piecha-Bisiorek, R. Jakubas, A. Cizman, J. K. Zaręba, M. Nyk, P. Zieliński, W. Medycki and A. Bil, *Chem. Mater.*, 2018, **30**, 4597–4608.

26 D. M. S. Martins, D. S. Middlemiss, C. R. Pulham, C. C. Wilson, M. T. Weller, P. F. Henry, N. Shankland, K. Shankland, W. G. Marshall, R. M. Ibberson, K. Knight, S. Moggach, M. Brunelli and C. A. Morrison, *J. Am. Chem. Soc.*, 2009, **131**, 3884–3893.

27 H. Ishida, Y. Furukawa, S. Sato and S. Kashino, *J. Mol. Struct.*, 2000, **524**, 95–103.

28 B. Bednarska-Bolek, R. Jakubas, G. Bator and J. Baran, *J. Mol. Struct.*, 2002, **614**, 151–157.

29 R. Jakubas, B. Bednarska-Bolek, J. Zaleski, W. Medycki, K. Hołderna-Natkaniec, P. Zieliński and M. Gałązka, *Solid State Sci.*, 2005, **7**, 381–390.

30 D. Nilsen, R. Larsen, K. Emerson, G. V Rubenacker, Z. Ping and J. E. Drumheller, *Inorg. Chem.*, 1990, **29**, 2887–2888.

31 M. Wei, R. D. Willett, D. Teske, K. Subbaraman and J. E. Drumheller, *Inorg. Chem.*, 1996, **35**, 5781.

32 Y. Zhang, W. Liao, D. Fu, H. Ye, M. Liu, Z. Chen and R. Xiong, *Adv. Mater*. 2015, **27**, 3942–3946.

33 Y. Zhang, W. Q. Liao, D. W. Fu, H. Y. Ye, Z. N. Chen and R. G. Xiong, *J. Am. Chem. Soc.*, 2015, **137**, 4928–4931.

34 M. Ksiądzyna, A. Gągor, A. Piecha-Bisiorek, A. Ciżman, W. Medycki and R. Jakubas, *J. Mater. Chem. C*, 2019, **7**, 10360–10370.

35 Y. Rechkemmer, F. D. Breitgoff, M. Van Der Meer, M. Atanasov, M. Hakl, M. Orlita, P. Neugebauer, F. Neese and B. Sarkar, and J. Van Slageren, *Nat. Commun.*, 2016, **7**, 10467–10474.

36 K. Chakarawet, P. C. Bunting and J. R. Long, *J. Am. Chem. Soc.*, 2018, **140**, 2058–206.

37 A. Eichhöfer, Y. Lan, V. Mereacre, T. Bodenstein and F. Weigend, *Inorg. Chem.*, 2014, **53**, 1962-1974.

38 J. M. Zadrozny and J. R. Long, *J. Am. Chem. Soc.*, 2011, **133**, 20732-20734.

39 J. M. Zadrozny, J. Liu, N. A. Piro, C. J. Chang, S. Hill and J. R. Long, *Chem.*

Commun., 2012, **48**, 3927-3929.

40 T. Jurca, A. Farghal, P. H. Lin, I. Korobkov, M. Murugesu and D. S. Richeson, *J. Am. Chem. Soc.*, 2011, **133**, 15814-15817.

41 F. Habib, O. R. Luca, V. Vieru, M. Shiddiq, I. Korobkov, S. I. Gorelsky, M. K. Takase, L. F. Chibotaru, S. Hill, R. H. Crabtree and M. Murugesu, *Angew. Chem., Int. Ed.*, 2013, **52**, 11290-11293.

42 D. M. Pinero Cruz, D. N. Woodruff, I. R. Jeon, I. Bhowmick, M. Secu, E. A. Hillard, P. Dechambenoit and R. Clérac, *New J. Chem.*, 2014, **38**, 3443-3448.

43 J. Vallejo, I. Castro, R. Ruiz-García, J. Cano, M. Julve, F. Lloret, G. De Munno, W. Wernsdorfer and E. Pardo, *J. Am. Chem. Soc.*, 2012, **134**, 15704-15707.

44 X. C. Huang, C. Zhou, D. Shao and X. Y. Wang, *Inorg. Chem.,* 2014, **53**, 12671-12673.

45 L. Chen, J. Wang, J. M. Wei, W. Wernsdorfer, X. T. Chen, Y. Q. Zhang, Y. Song and Z. L. Xue, *J. Am. Chem. Soc.,* 2014, **136**, 12213-12216.

46 A. E. Ion, S. Nica, A. M. Madalan, S. Shova, J. Vallejo, M. Julve, F. Lloret and M. Andruh, *Inorg. Chem.*, 2015, **54**, 16-18.

47 S. Vaidya, S. Tewary, S. K. Singh, S. K. Langley, K. Murray, Y. Lan, W. Wernsdorfer, G. Rajaraman and M. Shanmugam, *Inorg. Chem*., 2016, **55**, 9564—9578.

48 E. A. Suturina, J. Nehrkorn, J. M. Zadrozny, J. Liu, M. Atanasov, T. Weyhermueller, D. Maganas, S. Hill, A. Schnegg, E. Bill, J. R. Long and F. Neese, *Inorg. Chem*., 2017, **56**, 3102-3118.

49 A. K. Mondal, M. Sundararajan and S. A. Konar, *Dalton Trans*., 2018, **47**, 3745-3754.

50 J. M. Zadrozny, J. Telser and J. R. Long, *Polyhedron*, 2013, **64**, 209-217.

51 M. R. Saber and K. R. Dunbar, *Chem. Commun*., 2014, **50**, 12266-12269.

52 Agilent (2014). *CrysAlis PRO*. Agilent Technologies Ltd, Yarnton, Oxfordshire, England.

53 G. M. Sheldrick, *Acta Cryst. C*, 2015, **71**, 3e8.

54 O. V. Dolomanov, L. J. Bourhis, R. J. Gildea, J. A. K. Howard and H. Puschmann, *J. Appl. Crystallogr.*, 2009, **42**, 339–341.

55 J. D. Epperson, Li-June Ming, B. D. Woosley, G. R. Baker, and G. R. Newkome, *Inorg. Chem.*, 1999, **38**, 4498-4502.

56 B. Bednarska-Bolek, R. Jakubas, W. Medycki, D. Nowak and J. Zaleski, *J. Phys. Condens. Matter*, 2002, **14**, 3129–3142.

57 W. Medycki, J. Świergiel, K. Hołderna-Natkaniec, K. Jurga and R. Jakubas, *Solid State Nucl. Magn. Reson.*, 2004, **25**, 129–132.

58 R. Boča, *A Handbook of Magnetochemical Formulae*, Elsevier, Amsterdam, 2012.

59 C. Rajnák, A. Packová, J. Titiš, J. Miklovič, J. Moncol, R. Boča, *Polyhedron*, **2016**, 110, 85–92.

60 L. Smolko, J. Černák, M. Dušek, J. Miklovič, J. Titiš, R. Boča, *Dalton Trans*. **2015**, 44, 17565–17571.

61 A. Świtlicka, B. Machura, M. Penkala, A. Bieńko, D. C. Bieńko, J. Titiš, C. Rajnák, R. Boča, A. Ozarowski, *Inorg. Chem. Front*., 2020, **7**, 2637-2650.

62 R. Boča, J. Miklovič, J. Titiš, *Inorg. Chem*. **2014**, 53, 2367–2369.

63 C. Rajnák, J. Titiš, O. Fuhr, M. Ruben, R. Boča, *Inorg. Chem*. **2014**, 53, 8200−8202.

64 A. Świtlicka, B. Machura, M. Penkala, A. Bieńko, D. C. Bieńko, J. Titiš, C. Rajnák, R. Boča, A. Ozarowski, M. Ozerov, *Inorg. Chem*., 2018, **57**, 12740-12755.

65 K. Fukui, H. Ohya-Nishinuchi and N. Hirota, *Bull. Chem. Soc. Jpn*., 1991, 64, 1205-1212.

66 K. Fukui, N. Kojima, H. Ohya-Nishinuchi and N. Hirota, *Inorg. Chem*., 1992, **31**, 1338-1344.

67 D. Maganas, S. Milikisyants, J. M. A. Rijnbeek, S. Sottini, N. Levesanos, P. Kyritsis and E. J. J. Groenen, *Inorg. Chem*., 2010, **49**, 595-605.

68 D. Maganas, S. Sottini, P. Kyritsis, E. J. J. Groenen and F. Neese, *Inorg. Chem.,* 2011, **50**, 8741-8754.

69 S. Vaidya, A. Upadhyay, S. K. Singh, T. Gupta, S. Tewary, S. K. Langley, J. P. S. Walsh, K. S. Murray, G. Rajaraman and M. Shanmugam, *Chem. Commun*., 2015, **51**, 3739-3742.

70 S. Vaidya, S. Tewary, S. K. Singh, S. K. Langley, K. Murray, Y. Lan, W. Wernsdorfer, G. Rajaraman and M. Shanmugam, *Inorg. Chem*., 2016, **55**, 9564-9578.

71 S. Vaidya, S. K. Singh, P. Shukla, K. Ansari, G. Rajaraman, M. Shanmugam, *Chem. Eur. J.* 2017, **23**, 9546 – 9559.